Cement and Concrete Research 140 (2021) 106321

Contents lists available at ScienceDirect

Cement and Concrete Research

journal homepage: www.elsevier.com/locate/cemconres

Effect of polycarboxylate ether on the expansion of ye'elimite hydration in the presence of anhydrite

Chen Li [a,b], Jiaqi Li [b], Antonio Telesca [c], Delphine Marchon [b,d], Ke Xu [b], Milena Marroccoli [c], Zhengwu Jiang [a,*], Paulo J.M. Monteiro [b]

[a] Key Laboratory of Advanced Civil Engineering Materials of Ministry of Education, School of Materials Science and Engineering, Tongji University, Shanghai 201804, China
[b] Department of Civil and Environmental Engineering, University of California, Berkeley, CA 94720, USA
[c] School of Engineering, University of Basilicata, Potenza 85100, Italy
[d] 8049 Zürich, Switzerland

ARTICLE INFO

Keywords:
$3CaO{\cdot}3Al_2O_3{\cdot}CaSO_4$ (D)
High-range water reducers (D)
Expansion (C)
Backscattered electron imaging (B)
Crystallization pressure

ABSTRACT

Polycarboxylate ether (PCE), a commonly used superplasticizer, is known to influence the morphology of ettringite during the early hydration of C_3A- and ye'elimite-containing cements. According to existing theories, such morphological changes may be crucial to the expansive behavior of these cements. This paper studied the expansion of ye'elimite-anhydrite pastes and found the use of PCE to reduce expansion after 4 days of curing. Hydration studies were conducted by calorimetry, X-ray diffractometry, scanning electron microscopy, mercury intrusion porosimetry, inductively coupled plasma–optical emission spectrometry, and X-ray microtomography. The results show that the influences of PCE on the morphology of ettringite and the hydration of ye'elimite were quite small after 2 days. Based on the crystal growth theory, the range of pores in which ettringite can grow was calculated to explain the observed expansive behaviors. The presence of ettringite nano-crystals in aluminum hydroxide was also revealed and considered as a possible expansion mechanism.

1. Introduction

Ye'elimite, also known as calcium sulfoaluminate, is the main phase in calcium sulfoaluminate (CSA) cements. It hydrates to form ettringite and monosulfate in the presence and absence of $CaSO_4$, respectively [1–4] (see Eqs. (1) and (2)).[1] The former reaction may induce expansion [5,6]; therefore, CSA cements can be used as expansive binders or expansive compounds in Portland cements [7,8]. By adjusting the $CaSO_4$ to ye'elimite molar ratio (termed as *M* ratio, *M*) in CSA cements, hydration reaction (1) occurs in different proportions, and thus the expansive behavior of CSA cements can be tuned. CSA cements can be used for rapid hardening and high-strength purposes when $M < 1.5$, for expansive purposes when $1.5 < M < 2.5$, and for self-stressing purposes when $M > 2.5$ [9–11].

$$C_4A_3\overline{S} + 2C\overline{S} + 38H \rightarrow C_6A\overline{S}_3H_{32} + 2AH_3 \quad (1)$$

$$C_4A_3\overline{S} + 18H \rightarrow C_4A\overline{S}H_{12} + 2AH_3 \quad (2)$$

Although the expansive character of CSA cements is attributed to the formation of ettringite (Eq. (1)), the existing literature has shown that the measured expansion does not coincide well with the amount of ettringite formed [5–7,12–15]. From a practical view, in addition to the *M* ratio, the expansion property is influenced by several other factors, e.g. water to cement ratio [16], type of $CaSO_4$ (anhydrite, bassanite, or gypsum) [17,18], particle size of cement [16,19], presence of lime [20–22], alkalinity in the pore solution [23,24], and utilization of supplementary cementitious materials [7,12].

Many theories have been put forward to model the expansive behavior at the micro-scale. Among these theories, the most well-known schools of thought are the "swelling" theory and the "crystal growth" theory. The swelling theory proposes that the reaction of ye'elimite and gypsum in the presence of calcium hydroxide forms colloidal ettringite. This type of ettringite can attract large amounts of water and thus expand due to inter-particle repulsion [21]. The crystal growth theory, however, suggests that the expansion is due to the growth of confined crystals from supersaturated solutions [25,26]. In the case of CSA

* Corresponding author.
E-mail address: jzhw@tongji.edu.cn (Z. Jiang).
[1] Cement notation:A = Al_2O_3, C = CaO, H = H_2O,$\overline{S}$ = SO_3

https://doi.org/10.1016/j.cemconres.2020.106321
Received 26 April 2020; Received in revised form 31 October 2020; Accepted 25 November 2020
Available online 10 December 2020

cement hydration, it is believed that the supersaturation with respect to ettringite not only influences the crystallization pressure generated by the growth of ettringite, but also determines the minimum size of pores which ettringite can grow in [6]. Significant expansion and cracking can occur when tensile stress, generated by the growth of ettringite, exceeds the strength of the matrix [6,7]. This theory is widely accepted by recent studies investigating the expansive behavior of CSA cements [6,7,14,27,28]. It has also been applied to explain the expansion of Portland cement concrete due to delayed ettringite formation (DEF) [29,30] and external sulfate attacks [31–33]. In addition to the expansion induced by ettringite formation, the "crystal growth" theory also helps to understand the salt damage (e.g., Na_2SO_4) of stones and masonries [34–36].

Although both the "swelling" and the "crystal growth" theories proposed distinct expansion mechanisms, they both state that the morphology of ettringite can affect the expansive behavior [37]. According to the "swelling" theory, a colloidal morphology refers to small size and high aspect ratio of ettringite crystals [21], whereas according to the "crystal growth" theory, the stress exerted by a growing crystal on the pore wall depends also on the size of the pore and thus on the crystal growing inside [25,26,30,38]. A recent study reported that the use of polycarboxylate ether (PCE) in CSA cement paste can reduce the size of ettringite crystals forming at early ages (60 min) [39]. Commonly used PCE superplasticizers are comb-shaped copolymers. In Portland cement systems, they are known to preferentially adsorb on aluminate phases that have a positively charged surface and modify the rheological behavior of the fresh mix by producing steric repulsive forces between the anhydrous and hydrated cement particles [40–43]. The adsorption of PCE on ettringite inhibits the growth of ettringite crystals and favors their nucleation [40,44,45]. As a result, in the presence of PCEs, ettringite crystals usually show smaller sizes and/or different aspect ratios compared with the situation when PCE is absent. Such an effect not only occurs in CSA cement systems, but also in the scenarios of Portland cement hydration [42,46], C_3A hydration [44,47], and synthesized ettringite (by spontaneous crystallization) [48,49].

The effects of PCE on the hydration and rheological properties of CSA cements have been well investigated in [46,50–54]. However, it remains still unknown whether the morphological changes on ettringite during the early hydration (60 min) [39] remain in the later ages and may influence the expansive behavior of CSA cements. In this paper the hydration behavior of ye'elimite-anhydrite pastes, with and without PCE, was studied. The morphology of ettringite, as well as the hydration and microstructural evolution of the pastes were studied by means of various investigation techniques. Based on the "crystal growth" theory, the effect of PCE on expansion was also analyzed.

2. Experimental

2.1. Materials

Ye'elimite was laboratory-synthesized by heating raw materials at 1300 °C and held for 60 min. An XRD study with Rietveld refinement showed that it consisted of 78% orthorhombic-ye'elimite, 20% cubic-ye'elimite, and 2% amorphous and unquantified phases. Anhydrite (99 wt%, Acros Organics) was used for the preparation of samples. The chemical compositions of ye'elimite and anhydrite (tested by X-ray fluorescence spectrometry) are shown in Table 1; the particle size distribution (tested by laser diffraction) is shown in Fig. 1. Deionized water was used for preparing the ye'elimite-anhydrite paste.

The PCE was synthesized by free radical copolymerization using methacrylic ester macromonomers (BASF) and methacrylic acid (Sigma-Aldrich). After the copolymerization, the polymer was ultrafiltered (Labscale TFF System, Merck Millipore) to remove residuals, macromonomers, and salts. The PCE molecular weight, determined by size exclusion chromatography (Agilent 1260 Infinity system), is 36,000 g/mol. The number of side chains in one molecule (n), calculated from the molecular weight, is equal to 27. The carboxylate to ether (C/E) ratio is 2.67. The number of ethylene oxide monomers in one side chain (P) is 23. The side chain molecular weight is 1000 g/mol.

Table 1
Chemical composition of ye'elimite and anhydrite, wt%.

	Ye'elimite	Anhydrite
Na_2O	<0.01	0.04
MgO	0.48	0.02
Al_2O_3	50.74	0.04
SiO_2	0.91	0.11
P_2O_5	0.18	0.01
SO_3	10.22	52.04
K_2O	0.04	<0.01
CaO	36.53	47.75
TiO_2	<0.01	<0.01
Fe_2O_3	0.18	<0.01
ZnO	0.02	<0.01
SrO	0.07	<0.01

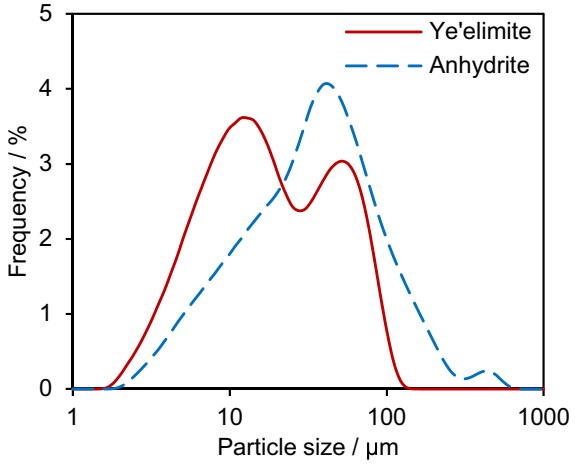

Fig. 1. Particle size distribution of ye'elimite and anhydrite.

2.2. Expansion tests

Expansion tests were conducted using pastes. The samples were labeled by their M ratio as M1.5, M2.0, M2.5, and M3.0. Both ye'elimite and anhydrite were firstly dry mixed for 3 min, and then mixed with either deionized water or PCE solution for 2 min. The PCE solution was prepared by mixing PCE with deionized water, and the PCE dosage was 0.2% (mass ratio of solid PCE to anhydrous powders). The water (excluding solid PCE) to binder (ye'elimite and anhydrite) ratio was 0.45.

The fresh pastes were cast into cylindrical plastic molds (6 cm in height and 1.27 cm in diameter). After casting, the samples were sealed by polytetrafluoroethylene (PTFE) films and cured at 23 °C. After 22 h, the samples were demolded and pre-conditioned in a fog room (RH > 95%) until reaching the 24th hydration hour. The initial length of each sample was measured by a caliper with a precision of ±0.01 mm. After that, two metal nuts were stuck onto the ends of each specimen by epoxy resin. The specimens were cured in deionized water (~5 mL for each cylinder) at 23 °C. The length change of the samples was measured by an extensometer with a precision of ±0.254 μm. For each mix proportion, three cylinders were prepared and measured. Some cylinders, belonging to the PCE-free groups, fractured during the tests. The length changes of these samples could not be measured by extensometer after fracturing; they were measured by means of a caliper, instead. The visual appearance of two sets of samples after 28 d expansion tests is shown in Fig. 2.

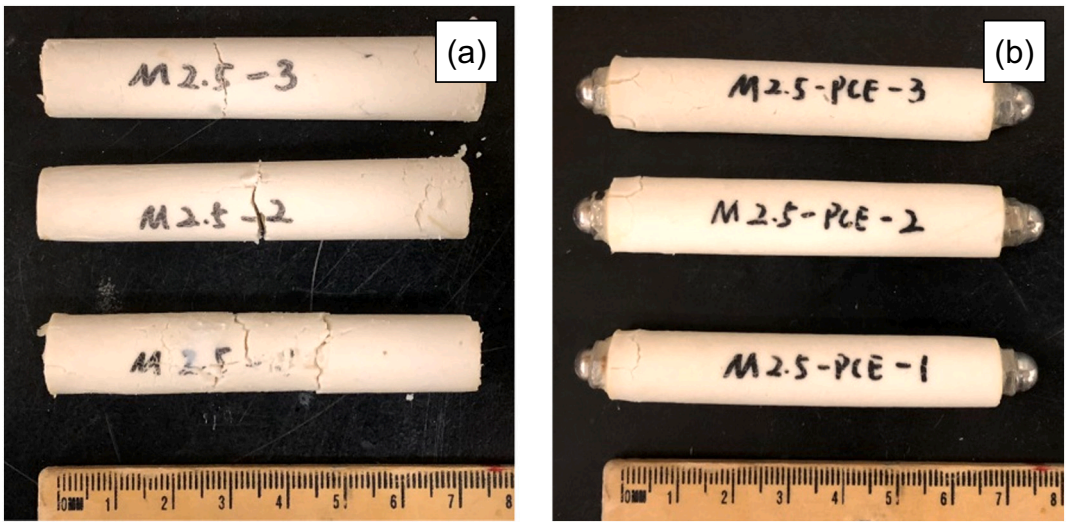

Fig. 2. Visual appearance of paste-samples prepared at an *M* ratio of 2.5, photographs taken after 28 d expansion tests: (a) Without PCE and (b) With PCE. The samples without PCE fractured during hydration. The scales on the ruler are in mm.

2.3. Hydration and microstructure study

The early age hydration was studied by isothermal conduction calorimetry on a TAM Air calorimeter (TA Instruments) operated at 23 °C. Six grams of anhydrous powders were employed for each test. The samples were mixed in ampoules outside the calorimeter according to the same mixing procedures described in Section 2.2.

For a better understanding of the hydration process and microstructure evolution of the pastes at different hydration ages, a new batch of samples was prepared and cured following the same procedures as those for the expansion tests. When reaching certain hydration ages, one part of the samples was ground into powders in isopropanol alcohol (Fisher Chemical) for both X-ray diffractometry (XRD) and thermogravimetric analyses (TGA). The others were sawed into small blocks with ~5 mm side length for scanning electron microscopy (SEM) observations and mercury intrusion porosimetry (MIP) measurements. The hydration of the powder samples and the blocks were stopped by the solvent exchange method using isopropanol. Afterward, the samples were dried in an oven at 40 °C for two days.

XRD was conducted on a PANalytical X'Pert PRO diffractometer equipped with X'Celerator position sensitive detector and iron filter, using Co Kα radiation. The X-ray generator was operated at 40 kV and 40 mA. The scanning range was $2\theta = 5–80°$. The step size was 0.0167°. The measured time for each scan was 2 h. Rietveld refinement was conducted by TOPAS Academic V5 using rutile (99.995%, Aldrich) as the external standard substance. The crystallographic models were obtained from the Inorganic Crystal Structure Database (ICSD, see Table 2). The optimized parameters included the background coefficient, zero-shift error, crystal size L, and lattice parameters. The peak shape was described by the fundamental parameter (FP) approach employed in TOPAS. The Rwp (Residual weighted profile) of the refinements was between 5% and 9% and the error of the refinements was estimated to be ~2%.

Table 2
Crystallographic models for Rietveld refinement.

Mineral	Chemical formula	ICSD code	Reference
Rutile	TiO_2	93097	[55]
Ye'elimite (orthorhombic)	$C_4A_3\overline{S}$	80361	[56]
Ye'elimite (cubic)	$C_4A_3\overline{S}$	9560	[57]
Anhydrite	$C\overline{S}$	15876	[58]
Gypsum	$C\overline{S}H_2$	409581	[59]
Ettringite	$C_6A\overline{S}_3H_{32}$	155395	[60]
Gibbsite	AH_3	6162	[61]

TGA was conducted on a Hitachi STA 7300 thermal analysis system. Approximately 20 mg powder sample was heated under N_2 atmosphere from 40° to 950 °C at a heating rate of 20 °C/min in an alumina crucible. The content of the chemically bound water, normalized to 100 g of unreacted powder was calculated according to Eq. (3). The mineralogical composition of the hydrated pastes, obtained from XRD analysis, was also normalized to 100 g of unreacted powders using the chemically bound water content, see Eq. (4).

$$W_n = \frac{M_{40} - M_{950}}{M_{950}} \tag{3}$$

$$W_{i,normal} = W_{i,Rietveld} \times (1 + W_n) \tag{4}$$

where W_n is the chemically bound water content; M_{40} and M_{950} are the masses of a specimen measured at 40° and 950 °C, respectively, during TGA; $W_{i,normal}$ is the normalized content of phase *i*; and $W_{i,Rietveld}$ is the content of phase *i* obtained from XRD Rietveld refinement.

The microstructure of the samples was observed by a Zeiss EVO MA10 microscope equipped with an energy dispersive X-ray spectrometry (EDS). The accelerating voltage and the beam current were 15 kV and 1 nA, respectively. The morphology of ettringite at early ages was observed using fractured samples on the secondary electron (SE) mode. The microstructure of the hardened pastes was investigated using polished samples impregnated in epoxy resin (EPO-TEK 301) on the backscattered electron (BSE) mode. The grinding and polishing processes were conducted using Bruker SiC grinding papers and diamond suspensions, respectively, to 25 μm fineness, and kerosene (Fisher Chemical) was used as a coolant. The samples for both SE and BSE analyses were carbon-coated.

The porosity of the samples was measured by a Thermo Finnigan Pascal 240 porosimeter which can reach a maximum pressure of 200 MPa. The porosimeter was equipped with a low-pressure unit (140 Series) that is able to generate a high vacuum level (10 Pa) and operate between 100 and 400 kPa.

2.4. Pore solution chemistry

Cylindrical samples (55 mm in diameter and ~15 mm in height) were prepared for the pore solution analyses. The pore solutions were extracted under a pressure of 30 MPa that was held for 2 min, followed by filtration with 0.45 μm nylon syringe filters (Acrodisc). The solutions

were acidified and diluted in 2 wt% nitric acid (prepared from 1 mol/L nitric acid, BDH) by a mass ratio of 1:10 and 1:100 [62], and stored at a 4 °C environmental chamber until analysis. The ionic composition of the solutions was measured by a Perkin Elmer inductively coupled plasma–optical emission spectrometry (ICP-OES). Standard solutions were prepared by diluting standards (Inorganic Ventures) in 2 wt% nitric acid.

The saturation index of ettringite was calculated by geochemical code GEMS 3.3 [63] with the Nagra/PSI database [64] and CEMDATA 18 database (version 18.01) [65]. It is defined as

$$SI = log_{10}\frac{Q}{K} \quad (5)$$

where, SI is the saturation index, Q is the ion activity product which is calculated based on the Debye-Hückel equation using the ionic composition determined by ICP-OES, and K is the solubility product under equilibrium conditions.

2.5. Synchrotron X-ray microtomography

Synchrotron X-ray microtomography (μCT) was conducted at beamline 8.3.2 at the Advanced Light Source (ALS) of the Lawrence Berkeley National Laboratory [66,67]. The beam energy was set to 35 keV with a constant beam current of 500 mA during the scans. For each scan, the sample was rotated around the axis perpendicular to the horizontal plane over 180°. 1969 projected radiographs were obtained over this rotation. Each projected radiograph was acquired through a 2× Mitutoyo magnification optical lens and a 2560px PCO_Edge CCD camera. The field of view was 8.8 mm and the spatial resolution was 3.3 μm/voxel. After each scan, the generated sinograms were reconstructed using the filtered back projection algorithm on Tomopy [68].

Cement paste samples, 6 mm in diameter and 20 mm in height, were prepared and cured following the same procedures as those for the expansion tests. After 10 days of curing, the samples were soaked in isopropanol for hydration stoppage. A 10-mm-high part was cut off from the middle of each sample and tested by μCT without drying. A stack of reconstructed images with 2560 × 2560 × 3000 voxels was obtained for each sample, and 1200 images in the middle of each stack were selected for visualization using Tomviz [69]. Image processing and segmentation were performed on Fiji [70]. A 3D bilateral filter (3 pixel size) [71] and a contrast enhancement with a saturated pixel of 0.35 were applied to eliminate the noise and improve the contrast between different phases [72,73]. To analyze the pore structure, the Moment-preserving [74] grey value threshold method embedded in Fiji was utilized to segment the pores and cracks from the solid phase (both anhydrous particles and hydration products), see Fig. 3. The porosity is defined as the percentage of pore voxels in the whole voxels of the testing sample. The connectivity of pores was analyzed based on a 6-connected voxel criterion, which means pore voxels are considered connected to form the "pore cluster/object" when the voxels share a common face with each other (pores are usually made of at least two voxels). Thus, pore connectivity (in %) is defined as the number of void voxels in the largest percolating pore object (cluster) divided by the total number of pore voxels in the testing sample [75,76]; it will be 100% when all of the pores in the system are percolating.

3D continuous pore size distribution was computed using the Xlib plugin in Fiji according to the method in [77]. It is based on the assumption that the pore network is a continuum and can be invaded by fluid as in MIP [77]. In this method, the pore objects (defined as spheres of identical volumes) are invaded from the largest pores to the smallest pores without considering the "ink bottle effect", and the continuous pore size distribution is defined as the relative volume of invaded spheres as a function of the sphere size [77].

3. Results

3.1. Expansion

Fig. 4 shows the expansion of the samples over time. The original length was measured at 1 d, and expansion was observed in all samples from 2 d. The expansion proceeded rapidly before ~14 d and subsequently slowed down. Among PCE-free samples (Fig. 4a), the M2.0 sample, prepared at the stoichiometric M ratio of Eq. (1), showed the largest total expansion at 28 d. Both M2.5 and M3.0 samples showed slightly smaller expansion, whilst M1.5 sample, where monosulfate may form stoichiometrically (Eq. (2)), showed the smallest expansion. The total expansion of the PCE-containing samples prepared at various M ratios (Fig. 4b) followed the same order as the PCE-free samples.

At a given M ratio, the samples with and without PCE showed comparable expansions before 4 d; later on, PCE-free samples expanded more than the PCE-containing samples. For PCE-free samples, the three cylindrical specimens tested in each series usually showed different expansion rates after 4 days of curing, though their final expansions were similar. Thus, the standard deviations on the expansion curves were high between 4 d and 14 d, but turned much smaller after 14 d. Between 7 d and 14 d, some of the specimens without PCE even fractured due to their large expansion (see Fig. 2b).

3.2. Hydration process

The fast dissolution of the anhydrous powders forms a strong initial exothermic peak in the heat flow curves, as shown in Fig. 5a and b. This initial peak was followed by an induction period. In PCE-free samples, the hydration reaction started to accelerate between 2 and 4 h. Two peaks can be observed in the main hydration period when the sources of water and sulfate for the precipitation of ettringite are believed to be

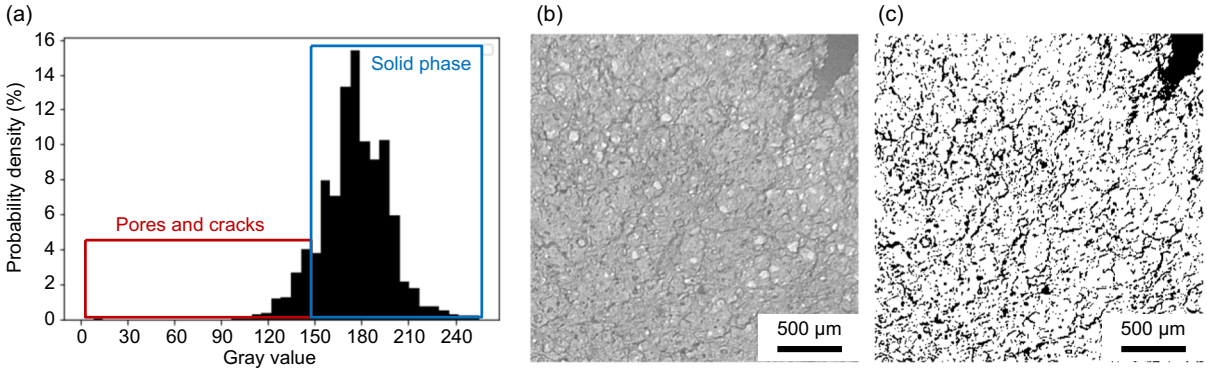

Fig. 3. Segmentation of pores and cracks in sample M2.0: (a) Grayscale histogram and thresholding of the Moment-preserving algorithm; (b) A preprocessed μCT image; and (c) The segmented image showing pores and cracks (black) and solid phase (white).

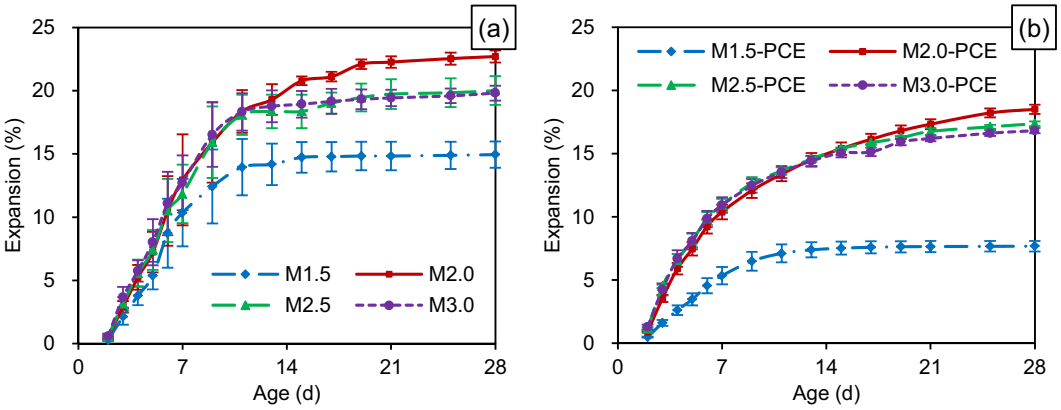

Fig. 4. Expansion of the samples: (a) Without PCE and (b) With PCE.

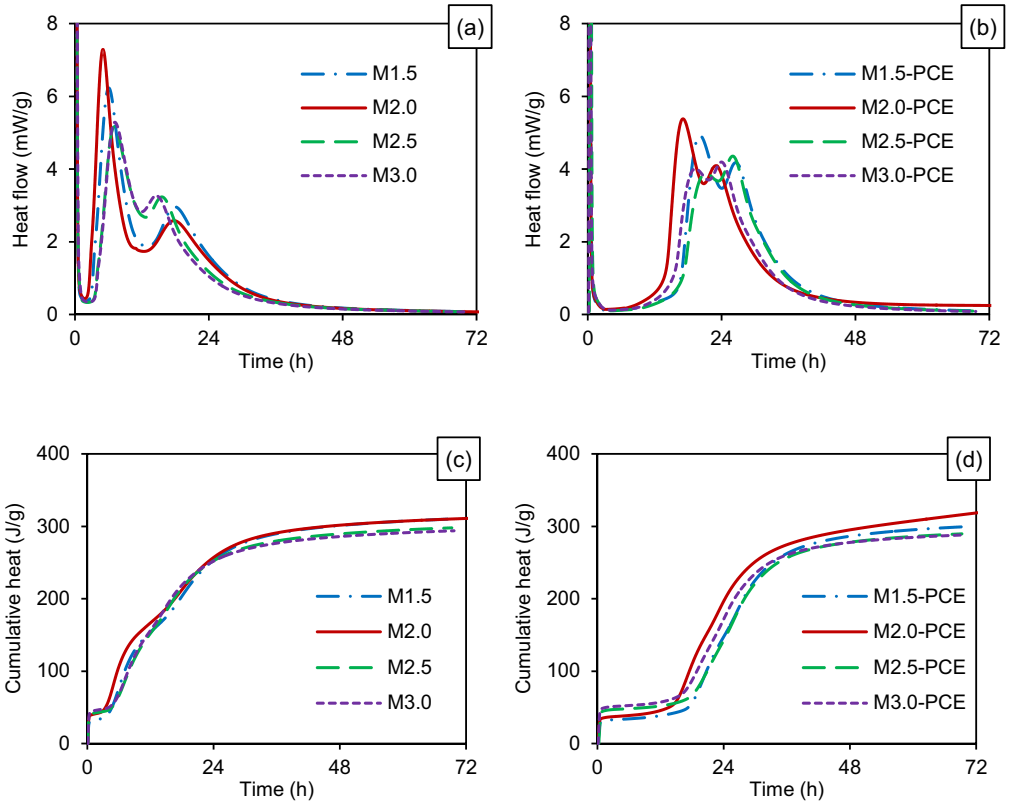

Fig. 5. Hydration heat normalized to the weight of anhydrous powders: (a) and (b) heat flow of the samples without PCE and with PCE, respectively; (c) and (d) cumulative heat of the samples without PCE and with PCE, respectively.

different [78]. M2.0 sample produced the highest hydration heat among the PCE-free samples. Compared with PCE-free samples, the acceleration period of the PCE-containing samples was retarded and appeared between 12 and 14 h. The first main hydration peak in the samples with PCE was lower than that in those without PCE; on the contrary, the second peak was higher.

The prolonged induction period brought by the use of PCE can be also observed on the cumulative heat curves (Fig. 5c and d). At a given *M* ratio, the cumulative heat of the sample with PCE turned almost equal to that of the PCE-free sample at 48 h and became slightly higher at 72 h. After the end of the expansion tests (28 d), the hydration of the cylinders was tested by TGA (Table 3). All the samples with PCE showed slightly higher chemically bound water content than the samples prepared at the same *M* ratio but without PCE. These results indicate that the retardation effect of PCE did not significantly influence the hydration process after the main hydration period.

Table 3
Chemically bound water content (mass %) measured by TGA. The samples were obtained from 28 d expansion tests.

M ratio	Chemically bound water	
	Without PCE	With PCE
M1.5	59.6	59.7
M2.0	67.4	71.4
M2.5	67.0	69.7
M3.0	64.3	67.7

The results above show that PCE reduces the expansion and retards

the early-age hydration (before 2 d) without influencing the long-term hydration (28 d) at all the investigated *M* ratios. To better understand the effect of PCE on the hydration and microstructure evolution, the samples prepared at the stoichiometric *M* ratio (M2.0 and M2.0-PCE) were studied in detail and are considered as representatives. The hydration products of these samples at different hydration ages were investigated by XRD and TGA, as shown in Table 4 and Fig. 6, respectively.

At 1d, PCE retarded the hydration of ye'elimite (Fig. 5). A larger amount of ye'elimite remained unreacted in the sample with PCE (XRD, Table 4), whilst smaller amounts of ettringite and aluminum hydroxide formed (Fig. 6a). Calcium sulfate is consumed by the hydration of ye'elimite and thus the sample with PCE showed much lower gypsum content at this hydration age (Table 4 and Fig. 6a). A small amount of anhydrite remained undissolved in both samples, and amorphous products (termed as Amorphous and Crystalline not-quantified, ACn [79,80]) were observed based on the XRD Rietveld refinements. At 4 d, the ye'elimite in PCE-containing sample hydrated to a slightly higher level compared with PCE-free sample (Table 4 and Fig. 6b). This phenomenon remained unchanged at both 7 d and 14 d.

3.3. Pore solution chemistry

The pore solution of the M2.0 samples showed high Ca and S concentrations relative to low Al concentration (Table 5). The Al concentration decreased during the hydration and reached ≤1 mmol/L after 7 d in both samples. These trends agree with [81] where the solution chemistry of a hydrated ye'elimite-anhydrite paste within the earliest 15 h was analyzed. The Na and K contents decreased over time; this phenomenon was also observed during the hydration of CSA cement [27].

At a given hydration age, PCE-free sample showed higher Na, K, S, and Al concentrations than PCE-containing sample, except at 1 d when the hydration was retarded by PCE. At 4 d and 7 d, when the samples expanded significantly, PCE-free sample also owed a higher Ca content. Thus, the PCE-free sample showed a higher saturation index of ettringite between 4 d and 14 d.

3.4. Pore structure

Fig. 7 shows the pore structure of the M2.0 samples. Without PCE (Fig. 7a), the sample showed a bimodal pore-radius distribution at the age of 8 h (main hydration period in calorimetry). At the age of 1 d, the pore-radius distribution became unimodal, with the threshold pore radius being ~20 nm. Afterward, the amount of the pores smaller than 20 nm decreased with the hydration time from 2 d till 7 d. A second peak near the radius of 20 nm seemed to form around 2 d, and it became quite clear at 4 d, creating a bimodal pore-radius distribution again. This peak became higher and moved toward a larger pore radius until 7 d.

It has been reported that hydrated CSA cement pastes usually shows a bimodal pore-radius distribution when $CaSO_4$ does not reach the stoichiometric molar ratio for ettringite formation (Eq. (1)), but a unimodal pore-radius distribution when $CaSO_4$ is sufficient [5,82]. In both situations, the pore volume decreases during the hydration, but the samples used in [5] were aircured in sealed bags and might not expand according to dimensional changes provided in that study. Considering that the intruded volume in MIP most properly represents the entry of a pore instead of the pore itself [83], the test results obtained here can be interpreted as follows: Before the 1st day of hydration, the amount of hydration products was insufficient to fill the space in the cement paste. Therefore, pores with large entries (~200 nm), representing the unhydrated areas, and pores with smaller entries (~40 nm), representing mainly the space in between hydration products, could both be observed. For curing periods longer than 1 d, most unhydrated areas are filled by hydration products. Thus, a unimodal pore-size distribution, similar to that of a CSA cement paste hydrated under a sufficient $CaSO_4$ content [5], formed. The continuous formation of hydration products, on one hand, fills part of the space, and the volume connected by small entries (<20 nm) turned even smaller. On the other hand, the expansion of the samples generated some cracks. As a result, some new open space connected by large entries was created again.

When PCE is added, the hydration of ye'elimite is retarded, and the pore-radius distribution remained bimodal at 1 d (Fig. 7b). Such a pore-radius distribution, as well as the high total pore volume relative to the PCE-free sample (compare Fig. 7d with Fig. 7c), indicates that the unhydrated areas (represented by the peak at ~600 nm) have not been fully filled by hydration products; this situation is similar to that of the PCE-free sample hydrated at 8 h (Fig. 7a) and coincides with the hydration processes influenced by the use of PCE (see calorimetry, Fig. 5). A unimodal pore-radius distribution formed at 2 d in the PCE-containing sample; however, the pore volume connected by entries smaller than ~10 nm was smaller than that of the sample without PCE. After 2 d, a bimodal distribution formed gradually; it is similar to the situation in the PCE-free sample. However, the volume connected by large pores (e.g. >20 nm) was smaller than that in the PCE-free sample, and the threshold pore radius was also smaller (Fig. 7c and d). These phenomena are consistent with the smaller expansion and fewer cracks generated thereby.

3.5. Microstructure

At 15 min of curing, the morphology of both ettringite and gypsum was similar (needle- or rod-like) (Fig. 8a and b), as it can be distinguished by EDS. Ettringite crystals formed in the presence of PCE were much finer than those formed in the absence of PCE. This result coincides with the finding in the spontaneous crystallization of ettringite in which the length and the diameter of ettringite both decreased with the increasing of the anodic charge amount of PCE [48].

Table 4
Hydration products assemblage (g) of M2.0 samples, normalized to 100 g anhydrous powders based on the chemically bound water (mass %) obtained by TGA. The overall errors after the Rietveld refinement and the normalization are estimated to be ±3%.

	Ye'elimite	Anhydrite[a]	Gypsum	Ettringite	Aluminum hydroxide	ACn	Chemically bound water
Without PCE M2.0							
1 d	30.7	5.0	25.0	45.2	12.4	14.2	32.5
4 d	19.5	–	20.5	74.8	22.6	8.9	46.4
7 d	14.1	–	13.3	92.9	28.6	2.4	51.3
14 d	7.5	–	7.8	113.8	32.3	0.5	61.8
With PCE M2.0-PCE							
1 d	58.2	7.8	37.2	5.1	0.4	2.5	11.1
4 d	12.4	–	16.2	92.6	25.0	5.6	51.9
7 d	8.2	–	10.4	105.0	29.1	5.1	57.8
14 d	5.0	–	4.6	125.9	33.5	−4.6[b]	64.5

[a] Anhydrite was not detected after 4 d and was not refined in the Rietveld analysis. Indicated by "–".
[b] A negative ACn value may be caused by the error of Rietveld analysis or TGA test, and can be considered to be ~0.

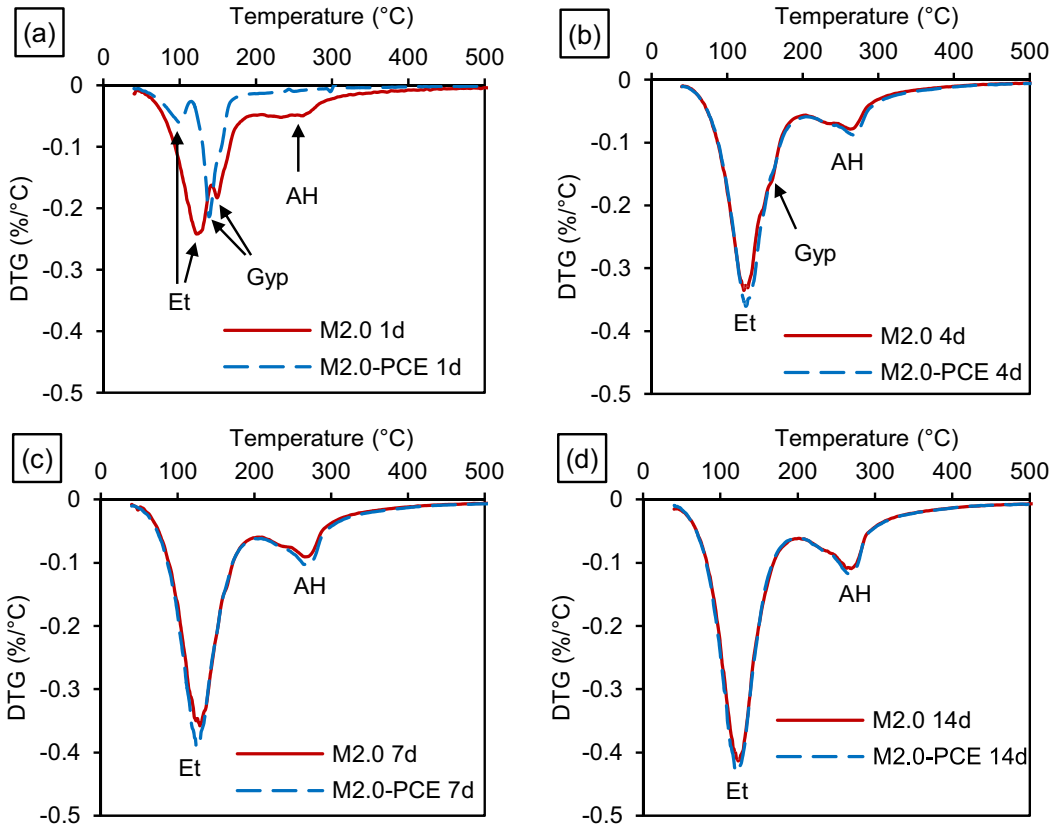

Fig. 6. Differential thermogravimetry (DTG) of M2.0 samples at different hydration ages: (a) 1 d, (b) 4 d, (c) 7 d, and (d) 14 d. Et = ettringite, Gyp = gypsum, and AH = aluminum hydroxide.

Table 5
Ionic composition (mmol/L, estimated error ±10%) of the pore solution measured by ICP-OES and saturation index of ettringite (−) calculated by GEMS.

	Ca	Na	K	S	Al	$SI_{Ettringite}$
Without PCE M2.0						
1 d	14.3	66.0	9.3	44.0	6.5	10.2
4 d	15.5	59.0	7.7	36.0	2.3	11.1
7 d	13.3	78.0	9.1	52.0	1.1	8.4
14 d	16.7	19.4	2.6	26.0	0.7	9.1
With PCE M2.0-PCE						
1 d	15.0	51.0	6.9	34.0	8.3	11.1
4 d	14.5	40.0	4.6	32.0	1.0	9.0
7 d	13.0	56.0	5.9	39.0	0.8	8.3
14 d	17.7	19.3	2.3	24.0	0.6	8.8

At 2 d, ettringite crystals in both samples showed similar morphology (Fig. 8c and d). Unreacted ye'elimite, ettringite, and aluminum hydroxide can be recognized. A few micro-cracks (~1–2 μm), most probably caused by the drying of the sample and the high vacuum in the SEM chamber [84], can be observed in the ettringite clusters; nevertheless, no significant differences can be found between the microstructures of both samples. Large cracks (several microns or larger) showed up at ~7 d (Fig. 8e and f). Till 14 d, more cracks were observed in PCE-free sample; they were larger than those in PCE-containing sample (Fig. 8g and h). A few ettringite crystals were also observed in the large cracks, especially in PCE-free sample. These ettringite crystals are much shorter than the width of the cracks. Therefore, it is unlikely that these crystals are responsible for the cracking. Besides, there is no evidence showing that the formation of the cracks may be induced by the growth of any large ettringite crystals inside or across them.

3.6. Cracking pattern

The 3D reconstructed images obtained by μCT show how the cracks form and propagate due to expansion (Fig. 9). Uniformly distributed cracks can be observed on the exterior surface of both samples (Fig. 9c and d); they were larger in size and more numerous than those inside the cylinders (Fig. 9e and f). In PCE-free sample, the width of the cracks ranged from ten to a few hundred micrometers. In comparison, most cracks in PCE-containing sample were smaller than 100 μm. 2D images on a cross-section of PCE-free sample (Fig. 10a and b) show the presence of large radical cracks (a few hundred microns in width) located on the exterior part of the sample, together with small cracks (tens of microns) forming all over the sample. The small cracks are consistent with SEM-BSE images reported in Fig. 8e and g. BSE images show that some of the large cracks on the exterior surface tend to propagate through the aluminum hydroxide–rich areas (Fig. 10d).

Both porosity and pore connectivity values of the PCE-free sample were higher than those of the PCE-containing one (Table 6), which confirms their expansive behavior. The smallest continuous pores that could be captured after image processing were 6.6 μm in radius (two pixels), and most pores in both samples were between 6.6 μm and 19.8 μm in radius (Fig. 11a). Within this range, the pore volume of the PCE-free sample was much larger than that of the PCE-containing one. Furthermore, larger pores (19.8 μm to 145 μm in radius) were also present in the PCE-free sample (Fig. 11b), which also coincides with the reconstructed images (Fig. 9).

3.7. Crystal growth in aluminum hydroxide

The aluminum hydroxide in the samples with and without PCE in their main hydration period (~0.8 h and ~1 d in calorimetry) showed

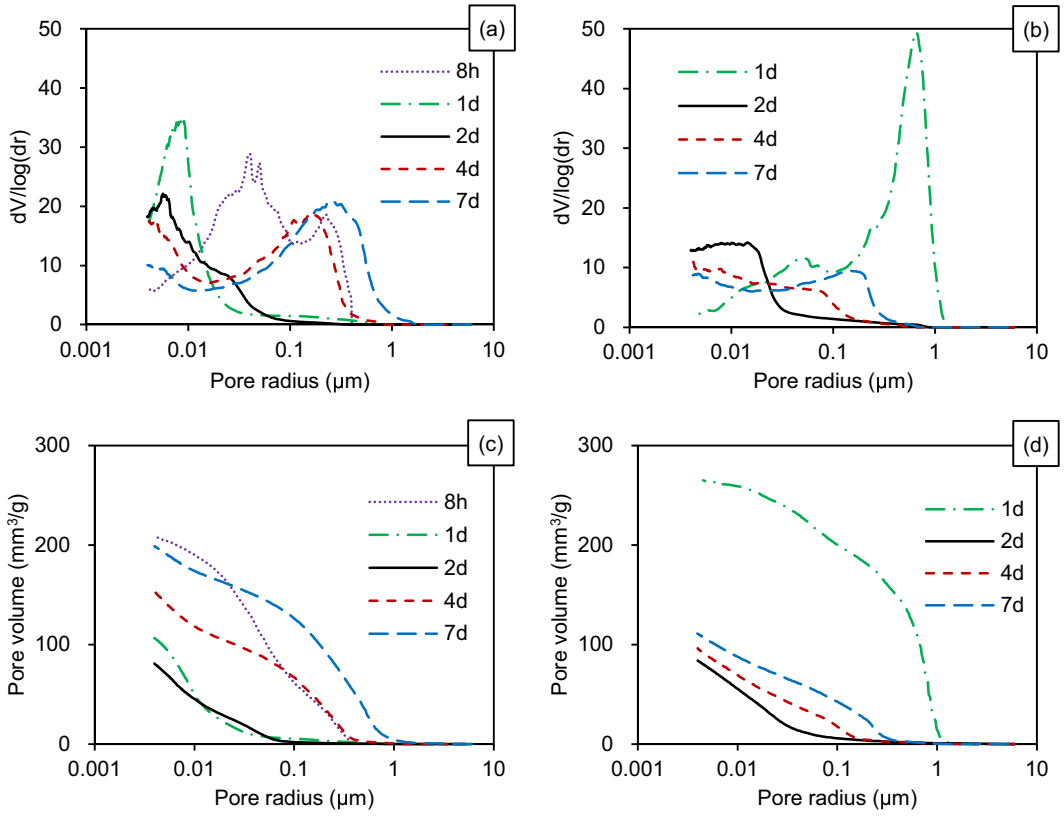

Fig. 7. Pore size distribution of M2.0 samples measured by MIP: (a) and (b) Derivative pore volume of the samples without PCE and with PCE, respectively; (c) and (d) Cumulative pore volume of the samples without PCE and with PCE, respectively.

similar features (Fig. 12a and e). A few needle-like crystals were embedded in the low-density aluminum hydroxide matrix. At 2 d (Fig. 12b and f), gypsum needle crystals (S/Ca = 0.85–1.05 by EDS) were apparently observed in the well-resolved aluminum hydroxide matrix. At 4 d, a few gypsum crystals remained in PCE-free sample (Fig. 12c), whereas few gypsum crystals were observed in PCE-containing sample (Fig. 12g). Inside the aluminum hydroxide matrix, small pores with sizes similar to the gypsum crystals could be observed in Fig. 12g. This fact indicates that the pores were left after the dissolution of the gypsum. At 7d, the gypsum embedded in the aluminum hydroxide matrix also disappeared in the PCE-free sample (Fig. 12d).

At the earliest hydration ages, the S/Ca of the aluminum hydroxide–rich region is 0.5–1.0, with the Al/Ca <2 (Fig. 12i). This fact suggests that the aluminum hydroxide is intimately intermixed with both gypsum (S/Ca = 1.0) and ettringite (S/Ca = 0.5). The S/Ca of the aluminum hydroxide matrix decreased to ~0.5 at 2 d (Fig. 12j) and then remained constant (Fig. 12k and l); this phenomenon suggests the presence of nano-sized ettringite inside the aluminum hydroxide matrix. The Al/Ca increased with the hydration age in both samples, indicating that the amount of ettringite inside the aluminum hydroxide matrix was decreasing. An apparent difference can be observed at 4 d when PCE-free sample showed a much higher Al/Ca than PCE-containing sample (Fig. 12k). This phenomenon coincides with the presence/absence of gypsum crystals embedded in the aluminum hydroxide matrix at the same hydration age (Fig. 12c and g). The compositions of the aluminum hydroxide matrix at different ages are summarized in Fig. 13.

4. Discussions

4.1. Effect of PCE on the morphology of ettringite and hydration of ye'elimite

In the C_3A-$CaSO_4$ systems, PCE promotes the homogeneous nucleation of ettringite [1,42,44]. The adsorption of PCE on ettringite restrains its growth [46], or even leads to the formation of ettringite nanocrystals with a particle size of 1–200 nm [47], thus increasing the specific surface area of the hydration products [44]. In the Portland cement systems, PCE is reported to reduce the aspect ratio of the ettringite crystals during the early hydration (10 s) [85]. It also retards the hydration of silicate by adsorbing on the anhydrous particles to prevent their dissolution [40,86,93].

The hydration of ye'elimite with $CaSO_4$ forms two generations of ettringite: one during the induction period and the other one during the main hydration period [81]. The growth of the ettringite formed in the induction period was restrained by PCE, as indicated by SEM observations (Fig. 8). And the main hydration period in the calorimetry was retarded (Fig. 4), which agrees with the effect of PCE on the hydration of CSA cements [46,50]. However, the morphological and dimensional differences of ettringite crystals between the samples with and without PCE became quite small at 2 d (SEM, Fig. 8). In agreement with the findings in CSA cement systems [51–53], the hydration degree of ye'elimite in both samples was also comparable after this hydration age (calorimetry, XRD and TGA). Since the influence of PCE on the expansion took place after 4 d, it is not likely that the different expansive behaviors between the samples with and without PCE are induced by the amount of ettringite or the morphology of ettringite crystals growing outside the aluminum hydroxide matrix.

Reference [17] proposed that the duration of plasticity can influence the expansive behavior of CSA cement mortars. In the present work,

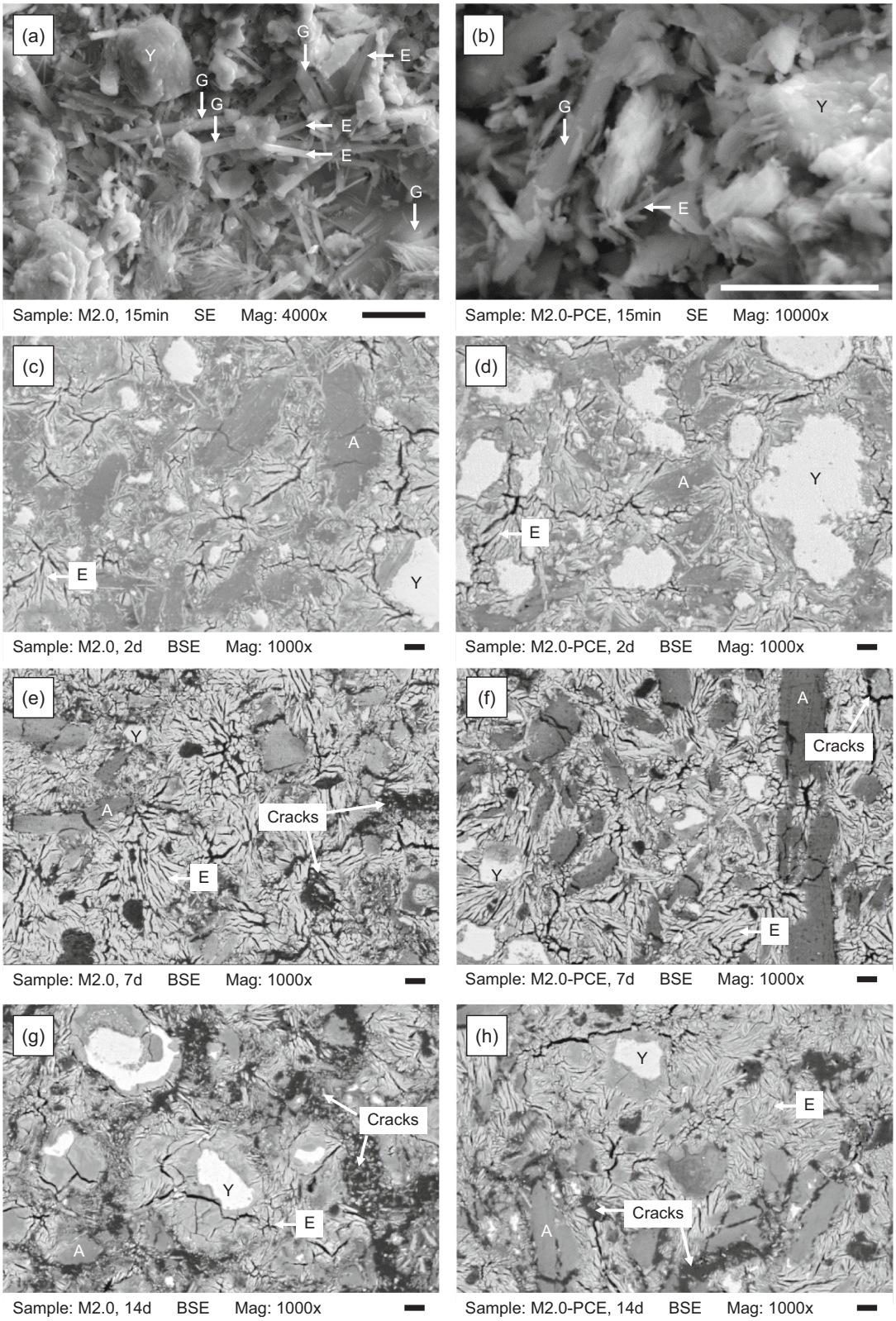

Fig. 8. Morphology of ettringite and microstructure of the samples observed by SEM: (a) and (b) 15 min SE images of M2.0 and M2.0-PCE, respectively; (c) and (d) 2 d BSE images of M2.0 and M2.0-PCE, respectively; (e) and (f) 7 d BSE images of M2.0 and M2.0-PCE, respectively; (g) and (h) 14 d BSE images of M2.0 and M2.0-PCE, respectively. The scale bars represent a length of 10 μm. G = gypsum, E = ettringite, A = aluminum hydroxide, and Y = ye'elimite. The darkest (black) regions in the BSE images refer to cracks impregnated by epoxy resin, and in subfigures (e), (g), and (f) there are also ettringite crystals (the small grey needles) growing inside the cracks.

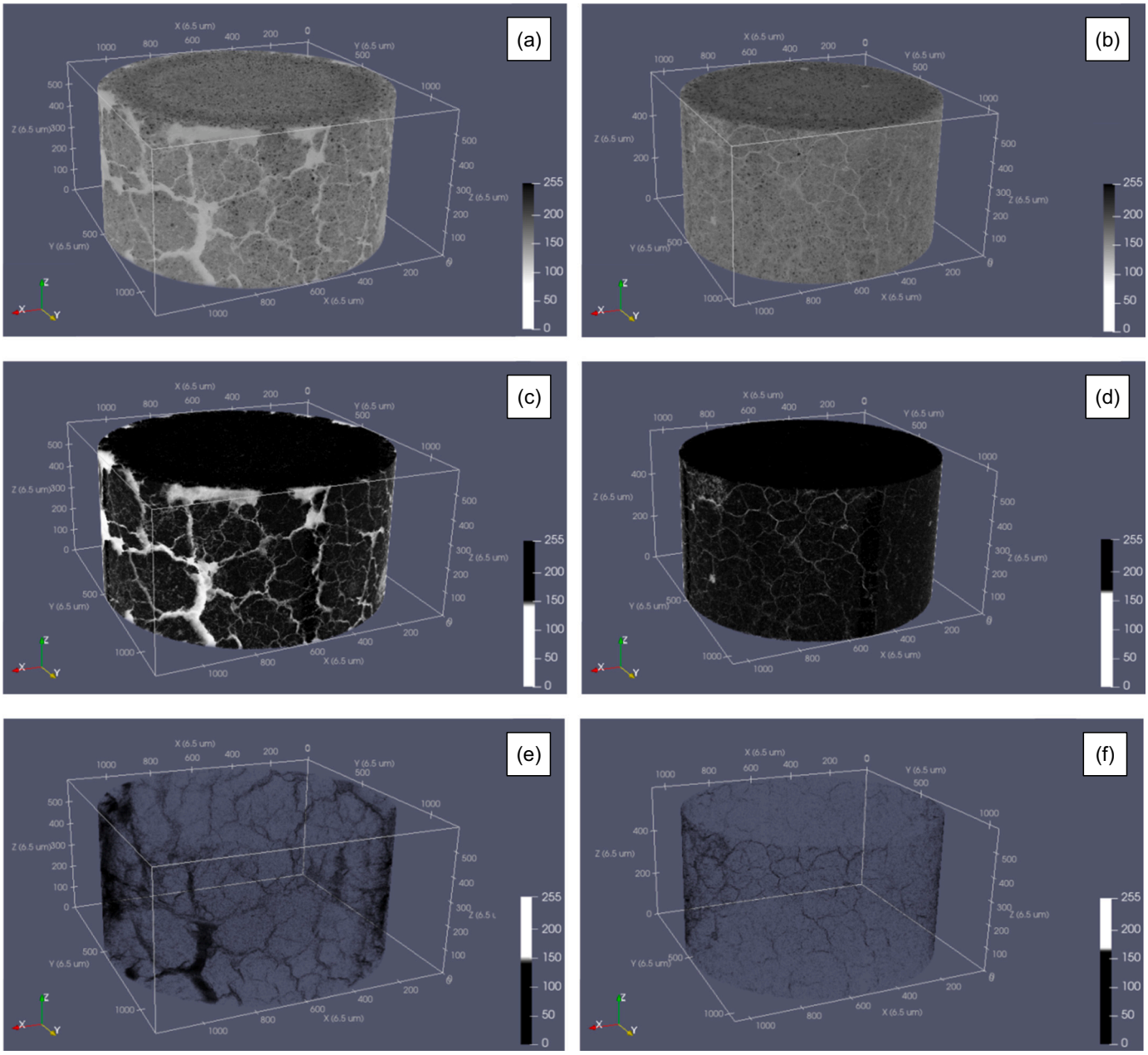

Fig. 9. Three-dimensional cracking pattern of the M2.0 samples obtained from μCT. The original diameter of the samples is 6 mm, and the height of the selected areas is 3.9 mm. The scales represent the number of pixels and each pixel is 6.6 μm in length. (a) and (b) Preprocessed images of the samples without PCE and with PCE, respectively; (c) and (d) Segmentation images showing cracks (white) and solid phase (black); (e) and (f) Segmentation images showing only cracks (black);

both samples with and without PCE lost plasticity before 1 d; however, the different expansive behavior had not been observed until 4 d (Fig. 4).

4.2. Range of pores for the growth of ettringite

The ICP-OES results indicate that the pore solution is supersaturated with respect to ettringite. Crystals growing in a confined pore space from a supersaturation solution can exert pressure on the pore walls [25,26]. Here, the range of pores in which ettringite can grow is firstly estimated according to [6], and the crystallization pressure generated therefrom is then analyzed.

The growth of a crystal can be driven by the supersaturation but restrained by the enlargement of the crystal-liquid interface. Provided that the crystal is spherical, it remains stable when these two effects are comparable [38], see Eq. (6).

$$\frac{RT}{v} ln\left(\frac{Q}{K}\right) = \gamma_{CL}\kappa_{CL} \tag{6}$$

where v (cm^3/mol) is the molar volume of the crystal, γ_{CL} (J/m^2) the interfacial free energy between the crystal and the liquid, and κ_{CL} (m^{-1}) the curvature of the crystal.

At a given supersaturation, a crystal tends to grow if its radius is above a critical value (percolated pore radius) but dissolves otherwise. Provided that ettringite crystal is percolating a cylindrical pore and a film of pore solution remains between the crystal and the pore wall, the pore radius can be calculated by Eq. 7 [87].

$$\kappa_{CL} = \frac{2}{r - \delta} \tag{7}$$

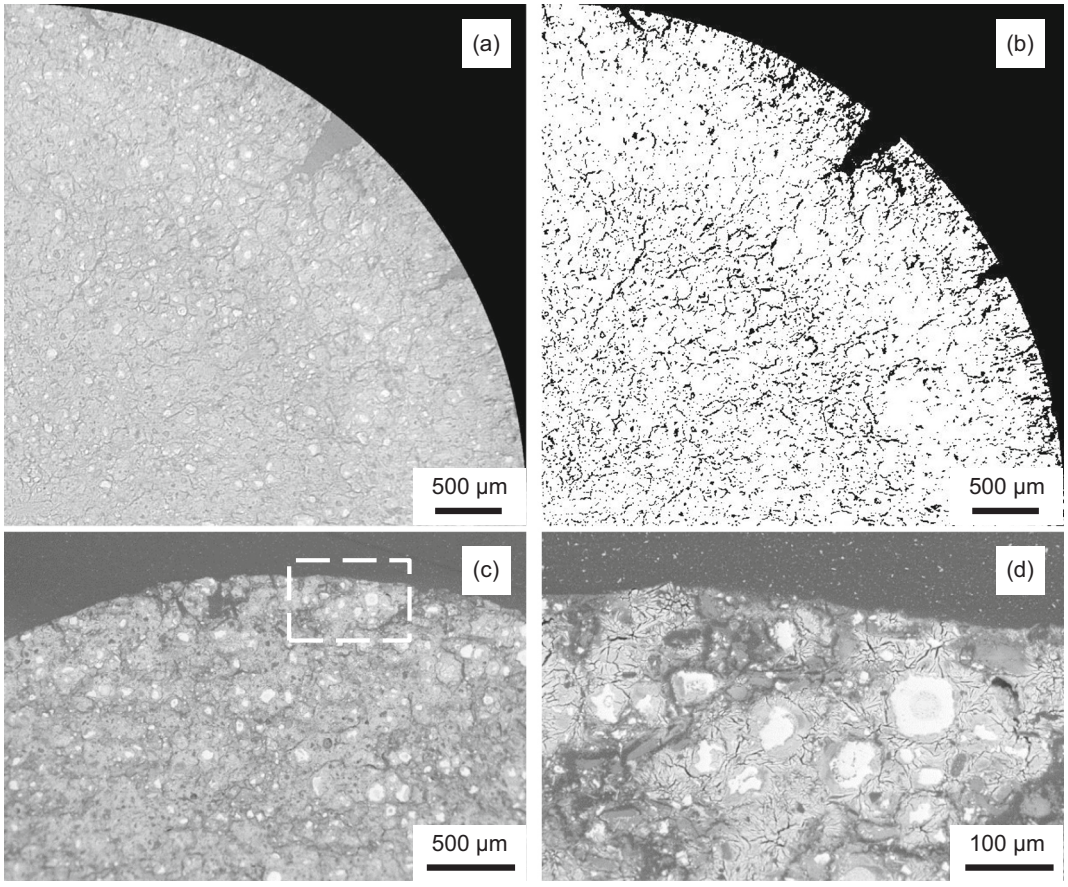

Fig. 10. Two-dimensional cross-section images obtained from the μCT of sample M2.0 (without PCE) and the SEM-BSE images of the same sample (different cross-section): (a) Preprocessed image obtained from μCT; (b) Segmentation image showing cracks (black) and solid phase (white) obtained from μCT; (c) SEM-BSE image; (d) An enlargement of the square area in sub-figure (c).

Table 6
Porosity (%) and pore connectivity (%) calculated from μCT.

	Porosity	Pore connectivity
M2.0	13.7	70.6
M2.0-PCE	5.7	54.0

where, r is the radius of the pore and δ is the thickness of the film.

When a crystal grows in a pore, the pressure produced by its growth is influenced by the structure of the pore network in addition to the supersaturation. For a spherical pore space connected by cylindrical entries, the area near the pore entry has a larger curvature than the main pore body. When the crystal near the pore entry is in equilibrium with the pore solution, the main crystal body will be supersaturated due to the curvature difference [30,34,38]. To suppress the growth of the main crystal body, an extra pressure has to be exerted by the pore wall, which can be calculated by Eq. (8) [5,30,38,88].

$$\Delta P = \frac{RT}{v} ln\left(\frac{Q}{K}\right) - \gamma_{CL}\kappa_{CL}^{C} = \gamma_{CL}\kappa_{CL}^{E} - \gamma_{CL}\kappa_{CL}^{C} \quad (8)$$

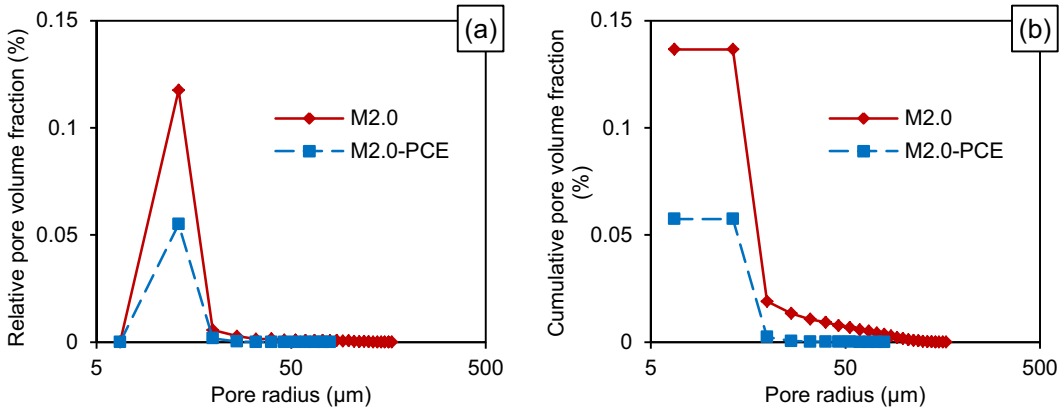

Fig. 11. Continuous pore size distribution calculated from the 3D segmented pore volumes of μCT, the minimum pore radius captured is 6.6 μm: (a) Relative distribution; and (b) Cumulative distribution.

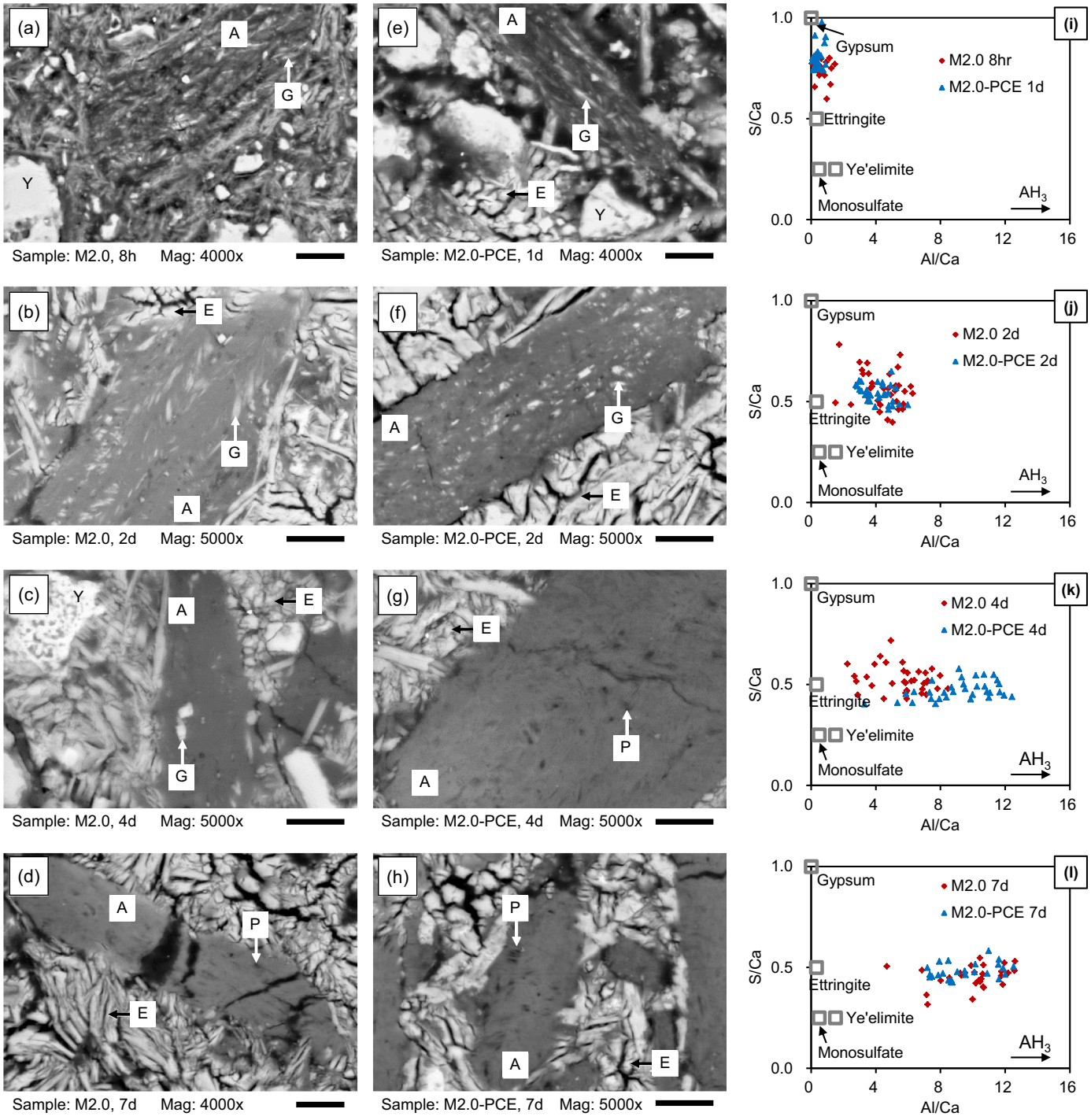

Fig. 12. Aluminum hydroxide observed by SEM-BSE and the chemical composition of the aluminum hydroxide matrix tested by EDS at the hydration ages of 0.8 h/1 d, 2 d, 4 d, and 7 d: (a) to (d) The SEM-BSE images of sample M2.0; (e) to (h) The SEM-BSE images of sample M2.0-PCE; (i) to (l) The chemical composition of the aluminum hydroxide matrix tested by EDS, the gypsum crystals embedded inside are avoided. The scale bars represent a length of 10 μm. G = gypsum crystals embedded in the aluminum hydroxide matrix, P = pores on the aluminum hydroxide matrix generated after the dissolution of gypsum, E = ettringite crystals growing outside aluminum hydroxide, A = aluminum hydroxide matrix, and Y = ye'elimite.

where, κ_{CL}^{E} and κ_{CL}^{C} represent the curvature of the pore entry and the main crystal body, respectively. If the radius of the main crystal body is much larger than that of the pore entry ($\kappa_{CL}^{C} \ll \kappa_{CL}^{E}$), the pressure that is exerted on the pore wall depends only on the radius of the pore entry and can be written as

$$\Delta P = \frac{RT}{v} ln\left(\frac{Q}{K}\right) = \gamma_{CL}\kappa_{CL}^{E} \quad (9)$$

Eq. (9) indicates that the maximum crystallization pressure generated by a single crystal depends on the radius of the pore entry. Crystals growth in pores with small entries usually generate high crystallization pressure; in addition, crystals growth in pores that are connected by entries of >0.1 μm in radius generate limited crystallization pressure [26,36]. On the macroscale, the tensile stress generated by the growth of crystals depends on both the crystallization pressure of a single crystal (Eqs. (8) or (9)) and the number of crystals that are exerting

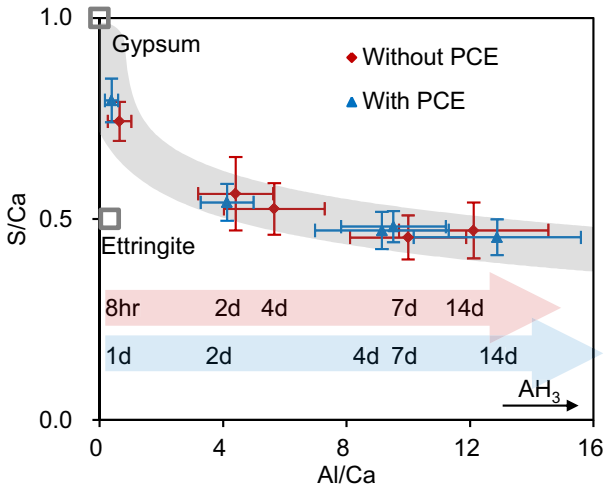

Fig. 13. The chemical composition of the aluminum hydroxide matrix at different hydration ages. Averaged based on the EDS analyses in Fig. 12.

crystallization pressure, which is expressed as Eq. (10) [6,29].

$$\sigma = P \cdot g(\varphi) \tag{10}$$

where, σ (MPa) is the tensile stress generated by the growth of crystals, φ (%) is the volume fraction of the crystals exerting crystallization pressure, and g(φ) is a geometric factor.

The percolated pore radius of ettringite (see Table 7) can be calculated by Eqs. (6) and (7) based on the saturation index obtained from ICP-OES (Table 5), and the pores measured by MIP in the present study can be further divided into three parts, see Fig. 14. The PCE-free sample owns more pore space in which the growth of ettringite can exert crystallization pressure (marked as II). More importantly, the pore volume which is connected by <10 nm entries was much larger in the PCE-free sample than in the PCE-containing sample. A similar phenomenon has also been reported in the CSA cement system that PCE reduced the pore space that is connected by entries smaller than ~20 nm [52]. The growth of ettringite in the pore space connected by nano-sized entries makes a greater contribution to the tensile stress than that in larger pores (Eqs. (9) and (10)), which can explain the different expansive behaviors between the samples with and without PCE.

4.3. Growth of ettringite in aluminum hydroxide matrix

Thermodynamically, crystals tend to grow in the open space to consume supersaturation rather than grow in the confined space to exert crystallization pressure [30]. When aluminum hydroxide started to form within 1 d, gypsum and ettringite crystals were wrapped inside (Fig. 12a and e). This phenomenon agrees with the transmission electron microscopy observations on the early hydration of CSA cement [89]. During the hydration, the gypsum embedded in the aluminum hydroxide matrix induces a high supersaturation with respect to ettringite, and thus the growth of ettringite in the confined space in aluminum hydroxide matrix will exert crystallization pressure. Alternatively, the Ca^{2+} and SO_4^{2-} in the aluminum hydroxide matrix can also diffuse outside the aluminum hydroxide matrix, promoting the growth of ettringite in the open space.

Table 7
Percolated pore radius estimated based on the saturation index of ettringite at 4 d. Parameters used for calculation: v = 705.8 cm^3/mol [6]; δ = 1.5 nm [6,38]; γ_{CL} = 0.1 J/m^2 [6,29].

	M2.0	M2.0-PCE
Saturation index of ettringite, $SI_{Ettringite}$ (−)	11.1	9.0
Percolated pore radius, r (nm ± 0.5)	3.8	4.3

This process consumes the supersaturation inside the aluminum hydroxide matrix, leading to the dissolution of gypsum, and is thermodynamically preferable. The results in Section 3.7 (Figs. 12 and 13) show that the growth of ettringite in the aluminum hydroxide matrix lasted longer in the PCE-free sample (from 2 d to 7 d) than in the PCE-containing sample (2 d to 4 d). This phenomenon can also explain the different expansive behaviors between the two samples.

Similar to the findings in the present paper, ettringite can grow in the mesopores in C-S-H, which has been proposed as the expansion mechanism for DEF [31,90,91]. The SO_4^{2-} produced by the destabilization of ettringite at elevated temperatures can be adsorbed by C-S-H [91,92]. The diffusion of ions from C-S-H toward the open space outside can theoretically take as long as several weeks [30,38]. After cooling to the room temperature, ettringite grows in the confined space in C-S-H, thus causing crystallization pressure and expansion [29,30]. This phenomenon is also confirmed in the scenario of external sulfate attack by [31,90] based on chemical composition analyses on C-S-H using SEM-EDS.

4.4. Duration of expansion

The expansion of the samples lasted till ~14 d. However, after 7 d the pores with an entry of <10 nm showed little difference between the sample with and without PCE (Fig. 7a and b), and the ettringite contents in the aluminum hydroxide matrix were also comparable in the two samples (Fig. 12). Similar phenomena can also be observed in the case of DEF that the expansion observed in the macroscale lasts for a longer duration compared with the supersaturation with respect to ettringite [30,38]. In terms of DEF, it is proposed that severe damage may occur in a short time, and expansion can take place under low crystallization pressure and thus tensile stresses afterward. This viewpoint is also verified by the fact that the maximum tensile strain that a concrete can sustain is usually smaller than 0.1%, whilst the expansion induced by DEF can reach the order of 1% [30,38].

The samples studied in this paper expanded to a much higher extent compared with those reported in the literatures studying the expansion of CSA cement systems [6,7,14,27,28]. It can be inferred that damage on the microscale may already form in the PCE-free sample around 4 d. Thus, this sample expanded more significantly than the PCE-containing sample after 7 d. The μCT images taken at 10 d also verified the presence of micro-damages in the PCE-free sample (Figs. 9 and 10). From 7 d to 14 d, the aluminum hydroxide matrix started to crack due to expansion (Figs. 10d and 12d). The Ca^{2+} and SO_4^{2-} in the aluminum hydroxide matrix could be released to the open space, and new ettringite crystals started to grow in the large cracks without confinement (see the small crystals in the cracks in Fig. 8e and g). Therefore, no further expansion is observed afterward.

5. Conclusions

At a given M ratio ($1.5 < M < 3.0$), PCE reduced the expansion of ye'elimite-anhydrite pastes after 4 d of curing. Hydration and microstructural studies on the samples with an M ratio of 2.0 revealed that PCE reduced the size of ettringite crystals forming during the induction period (15 min), and retarded the hydration before 2 d. After 2 d, the morphological difference of ettringite between the samples with and without PCE became quite small, and the two samples also hydrated comparably until 28 d.

PCE-free sample has more pore space in which ettringite can grow and exert crystallization pressure. Moreover, the pore space connected by nano-sized entries (<10 nm) is also larger in PCE-free sample than that in PCE-containing sample. The growth of ettringite in these nanopores can exert higher crystallization pressure compared with the growth of ettringite in larger pores, and thus induces higher tensile stress and larger expansion.

Nano-sized ettringite crystals can grow inside the aluminum

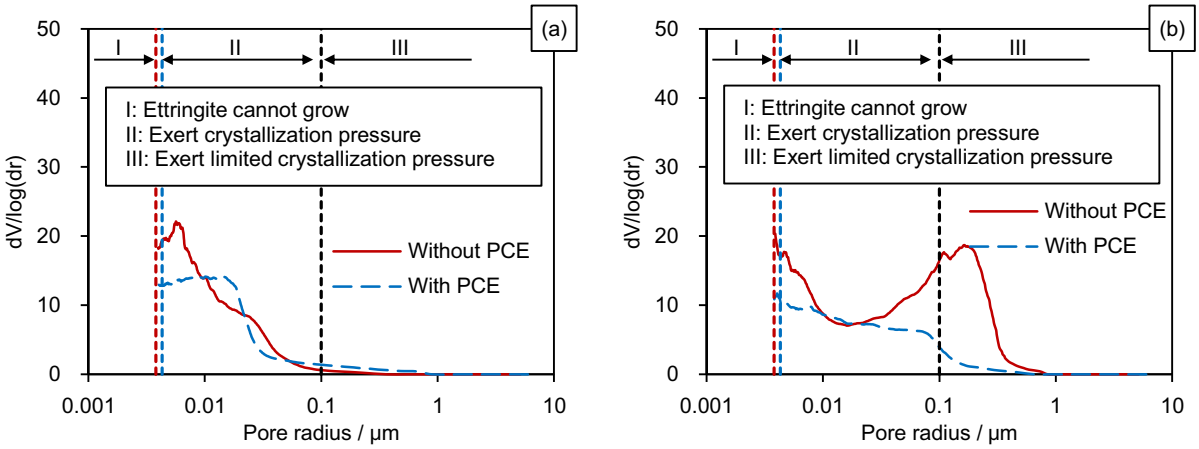

Fig. 14. Range of pores in which ettringite can grow and exert crystallization pressure: (a) M2.0 samples at 2 d; and (b) M2.0 samples at 4 d. The boundary between regions I and II is the percolated pore radius, see Table 7. The boundary between regions II and III is suggested by [26,36].

hydroxide matrix. Gypsum embedded in the aluminum hydroxide matrix can provide a high supersaturation with respect to ettringite, and thus the growth of ettringite in the confined space inside aluminum hydroxide can generate crystallization pressure. This process lasted for a longer time in PCE-free sample than in PCE-containing sample.

On one hand, provided that ettringite grows in all pores it can percolate, the reduced amount of nano-pores after PCE addition can be the reason for the smaller expansion. On the other hand, considering that the growth of ettringite in the confined space is not thermodynamically preferable, the smaller expansion after PCE addition can be attributed to the shortened duration of ettringite nano-crystals growing inside aluminum hydroxide. Both conclusions are drawn under the crystal growth theory and can explain the expansive behavior observed experimentally. The effect of PCE on the morphology of ettringite growing outside aluminum hydroxide matrix and that on the hydration of ye'elimite are not likely to coincide with the expansive behavior due to the short duration (within 2 d) of these effects.

Credit author statement

Chen Li: Methodology, Investigation, Data Curation, Writing - Original Draft, Writing - Review & Editing.

Jiaqi Li: Methodology, Investigation, Writing - Review & Editing.

Antonio Telesca: Investigation (MIP and ye'elimite synthesis), Writing - Review & Editing.

Delphine Marchon: Investigation (Calorimetry and PCE synthesis), Writing - Review & Editing.

Ke Xu: Investigation (μCT), Writing - Review & Editing.

Milena Marroccoli: Investigation (MIP and ye'elimite synthesis).

Zhengwu Jiang: Supervision, Methodology, Writing - Review & Editing.

Paulo J M Monteiro: Conceptualization, Methodology, Supervision, Writing - Review & Editing, Project administration, Funding acquisition.

Declaration of competing interest

The authors declare that they have no known competing financial interests or personal relationships that could have appeared to influence the work reported in this paper.

Acknowledgements

This work was supported by the Republic of Singapore's National Research Foundation – Berkeley Education Alliance for Research in Singapore (BEARS) for the Singapore-Berkeley Building Efficiency and Sustainability in the Tropics (SinBerBEST) Program. The authors (Zhengwu Jiang and Chen Li) gratefully acknowledge the financial support provided by National Key Research and Development Projects (2018YFC0705404), National Natural Science Foundation of China (51878480, 52078369), and the Fundamental Research Funds for the Central Universities. Financial support for Delphine Marchon was provided by the Swiss National Science Foundation (Early Postdoc.Mobility grant No. P2EZP2-172177). Chen Li acknowledges the financial support provided by China Scholarship Council (No. 201706260043). The Advanced Light Source is supported by the Director, Office of Science, Office of Basic Energy Sciences, of the U.S. Department of Energy under Contract No. DE-AC02-05CH11231. The authors thank Dula Parkinson for assistance with the μCT experiments, Michael Ngan, Wenxin Zhang, and Minju Zhong for assistance in sample preparations, Jun Li for assistance in particle size distribution analyses.

References

[1] F. Winnefeld, B. Lothenbach, Hydration of calcium sulfoaluminate cements — experimental findings and thermodynamic modelling, Cem. Concr. Res. 40 (2010) 1239–1247.

[2] C. Li, M. Wu, W. Yao, Eco-efficient cementitious system consisting of belite-ye'elimite-ferrite cement, limestone filler, and silica fume, ACS Sustain. Chem. Eng. 7 (2019) 7941–7950.

[3] C.W. Hargis, A.P. Kirchheim, P.J.M. Monteiro, E.M. Gartner, Early age hydration of calcium sulfoaluminate (synthetic ye'elimite, C_4A_3S) in the presence of gypsum and varying amounts of calcium hydroxide, Cem. Concr. Res. 48 (2013) 105–115.

[4] M. Ben Haha, F. Winnefeld, A. Pisch, Advances in understanding ye'elimite-rich cements, Cem. Concr. Res. 123 (2019) 105778.

[5] A. Telesca, M. Marroccoli, M.L. Pace, M. Tomasulo, G.L. Valenti, P.J.M. Monteiro, A hydration study of various calcium sulfoaluminate cements, Cem. Concr. Compos. 53 (2014) 224–232.

[6] J. Bizzozero, C. Gosselin, K.L. Scrivener, Expansion mechanisms in calcium aluminate and sulfoaluminate systems with calcium sulfate, Cem. Concr. Res. 56 (2014) 190–202.

[7] P. Chaunsali, P. Mondal, Physico-chemical interaction between mineral admixtures and OPC–calcium sulfoaluminate (CSA) cements and its influence on early-age expansion, Cem. Concr. Res. 80 (2016) 10–20.

[8] C.W. Hargis, B. Lothenbach, C.J. Müller, F. Winnefeld, Carbonation of calcium sulfoaluminate mortars, Cem. Concr. Compos. 80 (2017) 123–134.

[9] F. Winnefeld, S. Barlag, Calorimetric and thermogravimetric study on the influence of calcium sulfate on the hydration of ye'elimite, J. Therm. Anal. Calorim. 101 (2009) 949–957.

[10] C. Li, M. Wu, W. Yao, Effect of coupled B/Na and B/Ba doping on hydraulic properties of belite-ye'elimite-ferrite cement, Constr. Build. Mater. 208 (2019) 23–35.

[11] F. Winnefeld, B. Lothenbach, Phase equilibria in the system $Ca_4Al_6O_{12}SO_4$-Ca_2SiO_4-$CaSO_4$-H_2O referring to the hydration of calcium sulfoaluminate cements, RILEM Technical Letters. 1 (2016) 10–16.

[12] P. Chaunsali, P. Mondal, Influence of mineral admixtures on early-age behavior of calcium sulfoaluminate cement, ACI Mater. J. 112 (2015) 59–68.

[13] C.W. Hargis, A. Telesca, P.J.M. Monteiro, Calcium sulfoaluminate (ye'elimite) hydration in the presence of gypsum, calcite, and vaterite, Cem. Concr. Res. 65 (2014) 15–20.

[14] P. Chaunsali, P. Mondal, Hydration and early-age expansion of calcium sulfoaluminate cement-based binders: experiments and thermodynamic modeling, Journal of Sustainable Cement-Based Materials. 5 (2016) 259–267.
[15] L. Pelletier-Chaignat, F. Winnefeld, B. Lothenbach, C.J. Müller, Beneficial use of limestone filler with calcium sulphoaluminate cement, Constr. Build. Mater. 26 (2012) 619–627.
[16] I.A. Chen, C.W. Hargis, M.C.G. Juenger, Understanding expansion in calcium sulfoaluminate–belite cements, Cem. Concr. Res. 42 (2012) 51–60.
[17] M. García-Maté, A.G. De la Torre, L. León-Reina, E.R. Losilla, M.A.G. Aranda, I. Santacruz, Effect of calcium sulfate source on the hydration of calcium sulfoaluminate eco-cement, Cem. Concr. Compos. 55 (2015) 53–61.
[18] L. Pelletier-Chaignat, F. Winnefeld, B. Lothenbach, G.L. Saout, C.J. Müller, C. Famy, Influence of the calcium sulphate source on the hydration mechanism of Portland cement–calcium sulphoaluminate clinker–calcium sulphate binders, Cem. Concr. Compos. 33 (2011) 551–561.
[19] M. Cohen, C. Richards, Effects of the particle sizes of expansive clinker on strength-expansion characteristics of type K expansive cements, Cem. Concr. Res. 12 (1982) 717–725.
[20] W. Kurdowski, A. Thiel, On the role of free calcium oxide in expansive cements, Cem. Concr. Res. 11 (1981) 29–40.
[21] P.K. Mehta, Mechanism of expansion associated with ettringite formation, Cem. Concr. Res. 3 (1973) 1–6.
[22] D. Gastaldi, G. Paul, L. Marchese, S. Irico, E. Boccaleri, S. Mutke, L. Buzzi, F. Canonico, Hydration products in sulfoaluminate cements: evaluation of amorphous phases by XRD/solid-state NMR, Cem. Concr. Res. 90 (2016) 162–173.
[23] M.J. Sánchez-Herrero, A. Fernández-Jiménez, A. Palomo, $C_4A_3\bar{S}$ hydration in different alkaline media, Cem. Concr. Res. 46 (2013) 41–49.
[24] M. Deng, M. Tang, Formation and expansion of ettringite crystals, Cem. Concr. Res. 24 (1994) 119–126.
[25] M. Steiger, Crystal growth in porous materials—I: the crystallization pressure of large crystals, J. Cryst. Growth 282 (2005) 455–469.
[26] M. Steiger, Crystal growth in porous materials—II: influence of crystal size on the crystallization pressure, J. Cryst. Growth 282 (2005) 470–481.
[27] C.W. Hargis, B. Lothenbach, C.J. Müller, F. Winnefeld, Further insights into calcium sulfoaluminate cement expansion, Adv. Cem. Res. 31 (2019) 160–177.
[28] P. Chaunsali, P. Mondal, Influence of calcium sulfoaluminate (CSA) cement content on expansion and hydration behavior of various ordinary portland cement–CSA blends, J. Am. Ceram. Soc. 98 (2015) 2617–2624.
[29] R.J. Flatt, G.W. Scherer, Thermodynamics of crystallization stresses in DEF, Cem. Concr. Res. 38 (2008) 325–336.
[30] G.W. Scherer, Factors Affecting Crystallization Pressure, RILEM Publications SARL, Villars, Switzerland, International RILEM Workshop on Internal Sulfate Attack and Delayed Ettringite Formation, 2004, pp. 139–154.
[31] C. Yu, W. Sun, K. Scrivener, Mechanism of expansion of mortars immersed in sodium sulfate solutions, Cem. Concr. Res. 43 (2013) 105–111.
[32] W. Kunther, B. Lothenbach, K.L. Scrivener, On the relevance of volume increase for the length changes of mortar bars in sulfate solutions, Cem. Concr. Res. 46 (2013) 23–29.
[33] C. Li, Z. Jiang, R.J. Myers, Q. Chen, M. Wu, J. Li, P.J.M. Monteiro, Understanding the sulfate attack of Portland cement–based materials exposed to applied electric fields: mineralogical alteration and migration behavior of ionic species, Cem. Concr. Compos. 111 (2020) 103630.
[34] R. Flatt, N. Aly Mohamed, F. Caruso, H. Derluyn, J. Desarnaud, B. Lubelli, R. M. Espinosa-Marzal, L. Pel, C. Rodriguez-Navarro, G.W. Scherer, N. Shahidzadeh, M. Steiger, Predicting salt damage in practice: a theoretical insight into laboratory tests, RILEM Technical Letters. 2 (2017) 108.
[35] G.W. Scherer, R. Flatt, G. Wheeler, Materials science research for the conservation of sculpture and monuments, MRS Bull. 26 (2001) 44–50.
[36] R.M. Espinosa-Marzal, G.W. Scherer, Advances in understanding damage by salt crystallization, Acc. Chem. Res. 43 (2010) 897–905.
[37] G.L. Valenti, M. Marroccoli, M.L. Pace, A. Telesca, Discussion of the paper "Understanding expansion in calcium sulfoaluminate–belite cements" by I.A. Chen et al., Cem. Concr. Res. 42 (2012) 51–60, Cem. Concr. Res. 42 (2012) 1555–1559.
[38] G.W. Scherer, Stress from crystallization of salt, Cem. Concr. Res. 34 (2004) 1613–1624.
[39] H. Tian, X. Kong, Y. Cui, Q. Wang, D. Wang, Effects of polycarboxylate superplasticizers on fluidity and early hydration in sulfoaluminate cement system, Constr. Build. Mater. 228 (2019) 116711.
[40] A. Zingg, F. Winnefeld, L. Holzer, J. Pakusch, S. Becker, L. Gauckler, Adsorption of polyelectrolytes and its influence on the rheology, zeta potential, and microstructure of various cement and hydrate phases, J. Colloid Interface Sci. 323 (2008) 301–312.
[41] D. Marchon, P. Juilland, E. Gallucci, L. Frunz, R.J. Flatt, Molecular and submolecular scale effects of comb-copolymers on tri-calcium silicate reactivity: toward molecular design, J. Am. Ceram. Soc. 100 (2017) 817–841.
[42] F. Winnefeld, A. Zingg, L. Holzer, J. Pakusch, S. Becker, The Ettringite-Superplasticizer Interaction and its Impact on the Ettringite Distribution in Cement Suspensions, Ninth ACI international conference on superplasticizers and other chemical admixtures and tenth aci international conference on recent advances in concrete technology and sustainability issues, Seville, Spain, 2009, pp. 420.421–420.
[43] D. Marchon, F. Boscaro, R.J. Flatt, First steps to the molecular structure optimization of polycarboxylate ether superplasticizers: mastering fluidity and retardation, Cem. Concr. Res. 115 (2019) 116–123.
[44] F. Dalas, S. Pourchet, D. Rinaldi, A. Nonat, S. Sabio, M. Mosquet, Modification of the rate of formation and surface area of ettringite by polycarboxylate ether superplasticizers during early C_3A–$CaSO_4$ hydration, Cem. Concr. Res. 69 (2015) 105–113.
[45] P.J. Monteiro, G. Geng, D. Marchon, J. Li, P. Alapati, K.E. Kurtis, M.J.A. Qomi, Advances in characterizing and understanding the microstructure of cementitious materials, Cem. Concr. Res. 124 (2019) 105806.
[46] H. Tian, X. Kong, T. Su, D. Wang, Comparative study of two PCE superplasticizers with varied charge density in Portland cement and sulfoaluminate cement systems, Cem. Concr. Res. 115 (2019) 43–58.
[47] A. Lange, J. Plank, Formation of Nano-Sized Ettringite Crystals Identified as Root Cause for Cement Incompatibility of PCE Superplasticizers, Springer, 2015.
[48] M.R. Meier, A. Rinkenburger, J. Plank, Impact of different types of polycarboxylate superplasticisers on spontaneous crystallisation of ettringite, Adv. Cem. Res. 28 (2016) 310–319.
[49] M.R. Meier, J. Plank, Crystal growth of $[Ca_3Al(OH)_6{\cdot}12H_2O]_2{\cdot}(SO_4)_3{\cdot}2H_2O$ (ettringite) under microgravity: on the impact of anionicity of polycarboxylate comb polymers, J. Cryst. Growth 446 (2016) 92–102.
[50] T. Su, X. Kong, H. Tian, D. Wang, Effects of comb-like PCE and linear copolymers on workability and early hydration of a calcium sulfoaluminate belite cement, Cem. Concr. Res. 123 (2019) 105801.
[51] X. Yuan, W. Chen, M. Yang, Effect of superplasticizers on the early age hydration of sulfoaluminate cement, J. Wuhan Univ. Technol. Mater. Sci. Ed. 29 (2014) 757–762.
[52] M. García-Maté, I. Santacruz, Á.G. De la Torre, L. León-Reina, M.A.G. Aranda, Rheological and hydration characterization of calcium sulfoaluminate cement pastes, Cem. Concr. Compos. 34 (2012) 684–691.
[53] M. García-Maté, D. Londono-Zuluaga, A.G. De la Torre, E.R. Losilla, A. Cabeza, M. A.G. Aranda, I. Santacruz, Tailored setting times with high compressive strengths in bassanite calcium sulfoaluminate eco-cements, Cem. Concr. Compos. 72 (2016) 39–47.
[54] Y. Zhang, Z. Jiang, Y. Zhu, J. Zhang, Q. Ren, T. Huang, Effects of redispersible polymer powders on the structural build-up of 3D printing cement paste with and without hydroxypropyl methylcellulose, Constr. Build. Mater. 120551 (2020).
[55] P. Ballirano, R. Caminiti, Rietveld refinements on laboratory energy dispersive X-ray diffraction (EDXD) data, J. Appl. Crystallogr. 34 (2001) 757–762.
[56] N.J. Calos, C.H.L. Kennard, A.K. Whittaker, R.L. Davis, Structure of calcium aluminate sulfate $Ca_4Al_6O_{16}S$, J. Solid State Chem. 119 (1995) 1–7.
[57] H. Saalfeld, W. Depmeier, Silicon-free compounds with sodalite structure, Krist. Tech. 7 (1972) 229–233.
[58] G. Cheng, J. Zussman, The crystal structure of anhydrite ($CaSO_4$), Acta Crystallogr. 16 (1963) 767–769.
[59] J. Boeyens, V. Ichharam, Redetermination of the crystal structure of calcium sulphate dihydrate, $CaSO_4{\cdot}2H_2O$, Zeitschrift für Kristallographie-New Crystal Structures. 217 (2002) 9–10.
[60] F. Goetz-Neunhoeffer, J. Neubauer, Refined ettringite $(Ca_6Al_2(SO_4)_3(OH)_{12}{\cdot}26H_2O)$ structure for quantitative X-ray diffraction analysis, Powder Diffract. 21 (2006) 4–11.
[61] H. Saalfeld, M. Wedde, Refinement of the crystal structure of gibbsite, $Al(OH)_3$, Z. Kristallogr. Cryst. Miner. 139 (1974) 129–135.
[62] A. Vollpracht, B. Lothenbach, R. Snellings, J. Haufe, The pore solution of blended cements: a review, Mater. Struct. 49 (2016) 3341–3367.
[63] D.A. Kulik, T. Wagner, S.V. Dmytrieva, G. Kosakowski, F.F. Hingerl, K. V. Chudnenko, U.R. Berner, GEM-Selektor geochemical modeling package: revised algorithm and GEMS3K numerical kernel for coupled simulation codes, Comput. Geosci. 17 (2013) 1–24.
[64] W. Hummel, U. Berner, E. Curti, F. Pearson, T. Thoenen, Nagra/PSI chemical thermodynamic data base 01/01, Radiochim. Acta 90 (2002) 805–813.
[65] B. Lothenbach, D.A. Kulik, T. Matschei, M. Balonis, L. Baquerizo, B. Dilnesa, G. D. Miron, R.J. Myers, Cemdata18: a chemical thermodynamic database for hydrated Portland cements and alkali-activated materials, Cem. Concr. Res. 115 (2019) 472–506.
[66] Lawrence Berkeley National Laboratory Advanced Light Source Beamline 8.3.2. http://microct.lbl.gov.
[67] Beamline 8.3.2 Microtomography Manual, Advanced Light Source, Lawrence Berkeley National Laboratory (2015). http://microct.lbl.gov/manual.
[68] D. Gürsoy, F. De Carlo, X. Xiao, C. Jacobsen, TomoPy: a framework for the analysis of synchrotron tomographic data, J. Synchrotron Radiat. 21 (2014) 1188–1193.
[69] B.D. Levin, Y. Jiang, E. Padgett, S. Waldon, C. Quammen, C. Harris, U. Ayachit, M. Hanwell, P. Ercius, D.A. Muller, Tutorial on the visualization of volumetric data using tomviz, Microscopy Today. 26 (2018) 12–17.
[70] J. Schindelin, I. Arganda-Carreras, E. Frise, V. Kaynig, M. Longair, T. Pietzsch, S. Preibisch, C. Rueden, S. Saalfeld, B. Schmid, Fiji: an open-source platform for biological-image analysis, Nat. Methods 9 (2012) 676–682.
[71] D. Ushizima, K. Xu, P.J. Monteiro, Materials data science for microstructural characterization of archaeological concrete, MRS Advances. 5 (2020) 305–318.
[72] J. Li, W. Zhang, K. Xu, P.J. Monteiro, Fibrillar calcium silicate hydrate seeds from hydrated tricalcium silicate lower cement demand, Cem. Concr. Res. 137 (2020) 106195.
[73] K. Xu, A.S. Tremsin, J. Li, D.M. Ushizima, C.A. Davy, A. Bouterf, Y.T. Su, M. Marroccoli, A.M. Mauro, M. Osanna, Microstructure and Water Absorption of Ancient Concrete from Pompeii: An Integrated Synchrotron Microtomography and Neutron Radiography Characterization, arXiv preprint arXiv:2005.13114. (2020).
[74] W.-H. Tsai, Moment-preserving thresolding: A new approach, Computer Vision, Graphics, and Image Processing 29, 1985, pp. 377–393.
[75] N. Bossa, P. Chaurand, J. Vicente, D. Borschneck, C. Levard, O. Aguerre-Chariol, J. Rose, Micro-and nano-X-ray computed-tomography: a step forward in the

characterization of the pore network of a leached cement paste, Cem. Concr. Res. 67 (2015) 138–147.
[76] T. Sugiyama, M. Promentilla, T. Hitomi, N. Takeda, Application of synchrotron microtomography for pore structure characterization of deteriorated cementitious materials due to leaching, Cem. Concr. Res. 40 (2010) 1265–1270.
[77] B. Münch, L. Holzer, Contradicting geometrical concepts in pore size analysis attained with electron microscopy and mercury intrusion, J. Am. Ceram. Soc. 91 (2008) 4059–4067.
[78] D. Jansen, A. Spies, J. Neubauer, D. Ectors, F. Goetz-Neunhoeffer, Studies on the early hydration of two modifications of ye'elimite with gypsum, Cem. Concr. Res. 91 (2017) 106–116.
[79] G. Álvarez-Pinazo, A. Cuesta, M. García-Maté, I. Santacruz, E.R. Losilla, A.G.D. la Torre, L. León-Reina, M.A.G. Aranda, Rietveld quantitative phase analysis of Yeelimite-containing cements, Cem. Concr. Res. 42 (2012) 960–971.
[80] M. García-Maté, I. Santacruz, A. Cuesta, L. León-Reina, M.A.G. Aranda, I. Baco, V. Morin, G. Walenta, E. Gartner, Á.G. De la Torre, Amorphous determination in calcium sulfoaluminate materials by external and internal methods, Adv. Cem. Res. 27 (2015) 417–423.
[81] D. Jansen, J.J. Wolf, N. Fobbe, The hydration of nearly pure ye'elimite with a sulfate carrier in a stoichiometric ettringite binder system. Implications for the hydration process based on in-situ XRD, ^{1}H-TD-NMR, pore solution analysis, and thermodynamic modeling, Cem. Concr. Res. 127 (2020) 105923.
[82] G. Bernardo, A. Telesca, G.L. Valenti, A porosimetric study of calcium sulfoaluminate cement pastes cured at early ages, Cem. Concr. Res. 36 (2006) 1042–1047.
[83] S. Diamond, Mercury porosimetry: an inappropriate method for the measurement of pore size distributions in cement-based materials, Cem. Concr. Res. 30 (2000) 1517–1525.
[84] F. Bullerjahn, J. Skocek, M. Ben Haha, K. Scrivener, Chemical shrinkage of ye'elimite with and without gypsum addition, Constr. Build. Mater. 200 (2019) 770–780.
[85] M. Schönlein, J. Plank, Influence of PCE kind and dosage on ettringite crystallization performed under terrestrial and microgravity conditions, J. Am. Ceram. Soc. 101 (2018) 3575–3584.
[86] D. Jansen, J. Neubauer, F. Goetz-Neunhoeffer, R. Haerzschel, W.D. Hergeth, Change in reaction kinetics of a Portland cement caused by a superplasticizer — calculation of heat flow curves from XRD data, Cem. Concr. Res. 42 (2012) 327–332.
[87] G.W. Scherer, Crystallization in pores, Cem. Concr. Res. 29 (1999) 1347–1358.
[88] J. Houck, G.W. Scherer, Controlling stress from salt crystallization, in: S. K. Kourkoulis (Ed.), Fracture and Failure of Natural Building Stones, Springer, 2006, pp. 299–312.
[89] F. Song, Z. Yu, F. Yang, Y. Lu, Y. Liu, Microstructure of amorphous aluminum hydroxide in belite-calcium sulfoaluminate cement, Cem. Concr. Res. 71 (2015) 1–6.
[90] C. Yu, W. Sun, K. Scrivener, Degradation mechanism of slag blended mortars immersed in sodium sulfate solution, Cem. Concr. Res. 72 (2015) 37–47.
[91] H. Taylor, C. Famy, K. Scrivener, Delayed ettringite formation, Cem. Concr. Res. 31 (2001) 683–693.
[92] K. Tosun, B. Baradan, Effect of ettringite morphology on DEF-related expansion, Cem. Concr. Compos. 32 (2010) 271–280.
[93] Zhang Y., Jiang Z., Zhu Y., Zhang J., Ren Q., Huang T., Effects of redispersible polymer powders on the structural build-up of 3D printing cement paste with and without hydroxypropyl methylcellulose, Constr. Build. Mater., In press.